Moving discretized control set model-predictive control for dual-active bridge with the triple-phase shift

Chen, Linglin; Lin, Lyuyi; Shao, Shuai; Gao, Fei; Wang, Zhenyu; Wheeler, Patrick W.; Dragicevic, Tomislav

Published in:
IEEE Transactions on Power Electronics

DOI (link to publication from Publisher):
10.1109/TPEL.2019.2962838

Publication date:
2020

Document Version
Accepted author manuscript, peer reviewed version

This article has been accepted for publication in a future issue of this journal, but has not been fully edited. Content may change prior to final publication. Citation information: DOI 10.1109/TPEL.2019.2962838, IEEE Transactions on Power Electronics

Moving Discretized Control Set – Model Predictive Control for Dual-Active-Bridge with the Triple Phase Shift

Linglin Chen, Lyuyi Lin, Shuai Shao, *Member, IEEE*, Fei Gao, *Member, IEEE,* Zhenyu Wang, *Member, IEEE,* Patrick W. Wheeler, *Senior Member, IEEE* and Tomislav Dragicevic, *Senior Member, IEEE*

***Abstract*—Triple-Phase-Shift (TPS) is commonly utilized to enhance the efficiency of the Dual-Active-Bridge (DAB) converters. However, the small signal model of the circuit varies with operating mode, terminal voltage ratio and power. In order to address this issue, a control inspired by the finite control set - model predictive control is proposed. The proposed Moving Discretized Control Set - Model Predictive Control (MDCS-MPC) can achieve great control flexibility and good transition performance throughout the power and terminal voltage range with global control parameters. It presents fix switching frequency with low computational burden due to the utilization of only two prediction horizons. The operating principle of the proposed MDCS-MPC is introduced in development of a cost function that provides stiff load voltage regulation. The steady state error in MDCS-MPC has also been analyzed and compensated. The application of MDCS-MPC in a multi-objective control scenario has been addressed. Experiments on a 300V/300V 20kHz 1kW Dual-Active-Bridge converter are carried out to verify the theoretical claims.**

***Index Terms* — Dual-Active-Bridge (DAB), Model Predictive Control (MPC).**

NOMENCLATURE

f_s	Switching frequency
T_s	Time in one switching period
r_V	Terminal voltage ratio
V_{HV1}	Primary DC terminal voltage
V_{HV2}	Secondary DC terminal voltage
v_{ac1}	Primary transformer port voltage
v_{ac2}	Secondary transformer port voltage
D_1	Duty cycle of v_{ac1}
D_2	Duty cycle of v_{ac2}
D_f	Phase shift between v_{ac1} and v_{ac2}
L_p	Power transferring inductance on primary side
L_m	Transformer magnetizing inductance
C_{HV1}	DC capacitor on primary side
C_{VH2}	DC capacitor on secondary side
i_c	Current flowing into C_{HV2}
i_{ac2}	Transformer secondary current
i_{HV1}	Primary H-bridge DC side current
i_{HV2}	Secondary H-bridge DC side current
I_{load}	Load current
μ	Points to be calculated in T_s
μ_m	Maximum number of discretised elements
V_{HV2_ref}	Reference DC bus voltage
Δ_f	Finest step achievable by the digital control platform
Δ_{adp}	The adaptive step
G_1,G_2	Cost function terms
α_1, α_2	Weighting factors
I_{comp_f}	Prediction error compensation term

Manuscript received July 05, 2019 and revised November 09, 2019; accepted December 26, 2019. This work was supported in part by the Office of Naval Research Global under the award number N62909-17-1-2106. *(Corresponding authors: Shuai Shao, Fei Gao)*

L. Chen, Z. Wang and P. Wheeler are with the Department of Electrical and Electronics Engineering, University of Nottingham, Nottingham NG7 2RD, U.K. E-mail: (eexlc15; ezzzw1; eezpww) @nottingham.ac.uk.

L. Lin, S. Shao are with the College of Electrical Engineering, Zhejiang University, Hangzhou 310027, China. E-mail: shaos@zju.edu.cn.

F. Gao is with the Department of Electrical Engineering, Shanghai Jiao Tong University, Shanghai 200240, China. E-mail: fei.gao@sjtu.edu.cn.

T. Dragičević is with the Department of Energy Technology, Aalborg University, 9220 Aalborg East, Denmark. E-mail: tdr@ et.aau.dk.

I. INTRODUCTION

DC micro-grid has its applications in vehicles [1], vessels [2] and aircrafts [3] under the initiative of the transportation electrification. Energy Storage Systems (ESS) are often demanded in those system to provide intermittent power through the interface of isolated DC-DC converters. Dual-Active-Bridge (DAB) and its derived topologies [4]–[6] have drawn considerable attention in these applications [7], [8]. They provide salient merits in high frequency galvanic isolation, high voltage step up/down ability and high power conversion efficiency.

SPS is the most widely used modulation in the DAB due to its simplicity [9]–[12]. When the voltage gain deviates from unity, the SPS modulated DAB can have high circulating current and lose zero voltage switching (ZVS) on, which will decrease the efficiency significantly [13]. Various hardware and control methods have been proposed to solve these problems, among them, adjusting duty cycles of H-bridges are the most effective approach [13]. Based on the number of the phase shift ratios, these methods can be classified as extended phase shift (EPS) [14], dual phase shift (DPS) [15] and triple phase shift (TPS) [16]. Compared to EPS or DPS, the TPS utilizes all the three phase shift ratios and can maximize the efficiency.

In the existing literature, the control of DAB is mainly focused on the DAB modulated using the SPS (SPS-DAB) [17]–[21]. The control of TPS-DAB is barely addressed in the existing literatures due to its complexity. Since there are many different operating modes and three phase shift ratios, the variant small signal model of the TPS-DAB requires the PI controllers to be designed and tuned at each equilibrium points. Otherwise the performance will be deteriorated. The parameter design becomes complex when the converter has a wide operating voltage range. J. Huang *et al.*[22] employed two slow

This article has been accepted for publication in a future issue of this journal, but has not been fully edited. Content may change prior to final publication. Citation information: DOI 10.1109/TPEL.2019.2962838, IEEE Transactions on Power Electronics

PI controllers for the inner phase shifts to avoid oscillation and instability during transitions when using TPS. However, this significantly reduced the bandwidth of control. *K. Wu et al.*[23] addressed the stability issue with TPS using Lyapunov function. Each operating stage was treated separately which was inept at design guidance for the control parameters.

Predictive control is often considered in power electronics converters for several advantages it can provide, such as fast dynamics, easy inclusion of constraints, and simple digital implementation. In particular, Finite-Control-Set Model-Predictive-Control (FCS-MPC) has been investigated in AC power conversion [24]–[26]. In contrast, the application of predictive control in DC/DC converters has not been so intensively explored; FCS-MPC methods proposed for use in the boost converter with receding horizon by *P. Karamanakos et al*. [17] and *B. Wang et al*. [18] demonstrated fast dynamics. However, these approaches resulted in variable switching frequency and demanded heavy computation. *F. M. Oettmeier et al*. [19] proposed a Continuous-Control-Set Model-Predictive-Control (CCS-MPC) also for boost converters which effectively avoided voltage transition overshoot. Notwithstanding, above approaches are not applicable in TPS-DAB.

In this paper, the control variable in TPS-DAB is discretized into finite elements to fit in the concept of the well-known FCS-MPC. The proposed Moving-Discretized-Control-Set Model-Predictive-Control (MDCS-MPC) has the merits listed as follows:

1. Circuit parameters, terminal voltages and operating modes of TPS-DAB are embedded in the prediction model. Therefore, control parameters designed for MDCS-MPC can provide good performance throughout the power and terminal voltage range.

2. The proposed approach enables flexible multi-objective optimization. With the proposed method, similar DC micro-grid stabilization control typically seen with FCS-MPC can also be applied to TPS-DAB [27].

3. Compared to previous applications of FSC-MPC in DC-DC converters [17], [18], MDCS-MPC utilizes only two prediction horizon and a small number of calculating points in each switching period. Therefore, the computational burden is relatively low.

This paper is organised as follows: in Section II, the concept of TPS modulation is presented. The small signal modelling and the conventional PI control for TPS-DAB have been introduced. In Section III, the MDCS-MPC is proposed. The ideal discretised model is derived. Operating principle is intuitively introduced. The cost function and the adaptive step concept have also been set forth. Multi-objective control based on the proposed control concept is illustrated. In the next section, the causes of the steady state error for the proposed MDCS-MPC have been analysed in development of a compensation method. In Section V, experimental results are conducted on a 20kHz, 1kW DAB converter, validating theoretical claims. Section VI concludes the paper.

II. ANALYSIS ON TPS-DAB

The diagram of the Dual-Active-Bridge (DAB) converter is shown as in Fig. 1. H-bridges on each side of the high frequency transformer generate square voltages v_{ac1} and v_{ac2} with a fundamental frequency of f_s. They are exerted on the power transferring inductor L_p, producing transformer current i_{ac2}. T_s denotes one switching period.

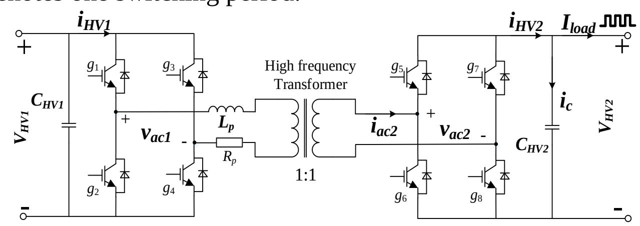

Fig. 1. The diagram of the DAB converter under investigation.

As depicted in Fig. 2, D_1T_s, D_2T_s are the active state time periods of v_{ac1} and v_{ac2}. When the SPS is applied [10], active states duties D_1 and D_2 are fixed at 0.5 while the phase shift D_fT_s between v_{ac1} and v_{ac2} is controlled to transfer the power between primary and secondary sides.

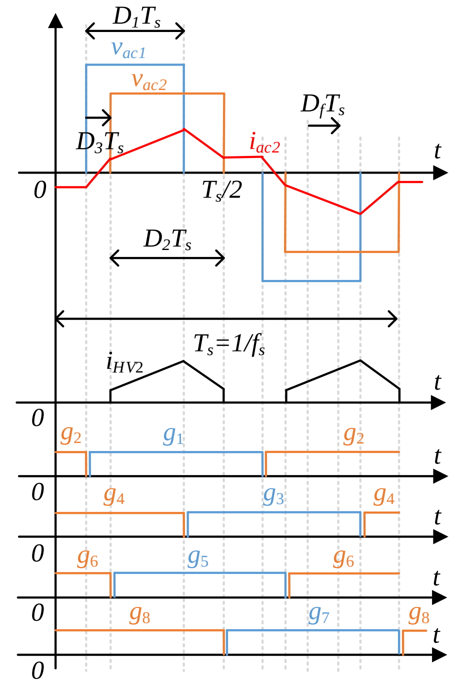

Fig. 2. Generic waveforms of the DAB modulated with TPS.

A. *Offline optimization on TPS-DAB*

The DAB converter has four control variables. They are D_1, D_2, D_f and f_s. In TPS, the phase shift ratios D_1, D_2 and D_f are regarded as three independent control variables while f_s is fixed. To minimize the circulating current, authors in [16], [28], [29] have derived the optimal phase shift ratios shown in Table I.

D_f is the only independent control variable, while D_1 and D_2 can be calculated using D_f. The gate signals g_1-g_8 can be then generated according to Fig. 2. Although the TPS modulation has its advantages, the complexity in control design hinders its application in practice. As shown in Table I, there are four operating modes, the small signal model of TPS-DAB varies with operating modes, terminal voltages and power.

This article has been accepted for publication in a future issue of this journal, but has not been fully edited. Content may change prior to final publication. Citation information: DOI 10.1109/TPEL.2019.2962838, IEEE Transactions on Power Electronics

TABLE I
MINIMIZATION ON REACTIVE POWER [16], $r_V = V_{HV2}/V_{HV1}$

Gain	D_f range	Relationships	Mode
$r_V<1$	$[0, \frac{1-r_V}{4}]$	$D_1 = \frac{2r_V}{1-r_V}D_f,\ D_2 = \frac{2}{1-r_V}D_f,\ D_3 = 0$	I
	$(\frac{1-r_V}{4}, \frac{1}{4}]$	$D_1 = \frac{2r_V-1}{2r_V} + \frac{1-r_V}{r_V}D_f,\ D_2 = 0.5,\ D_3 = \frac{r_V+4D_f-1}{4r_V}$	II
$r_V>1$	$[0, \frac{r_V-1}{4r_V}]$	$D_1 = \frac{2r_V}{r_V-1}D_f,\ D_2 = \frac{2}{r_V-1}D_f,\ D_3 = 2D_f$	III
	$(\frac{r_V-1}{4r_V}, \frac{1}{4}]$	$D_1 = 0.5,\ D_2 = 1-0.5r_V+2(r_V-1)D_f,$ $D_3 = (2-r_V)D_f + 0.25(r_V-1)$	IV

B. Modeling of the TPS-DAB

The accurate switching averaged models of the DAB have been intensively investigated by researchers [29], [30]. However, those models of DAB draw on the most straightforward SPS modulation. When it comes to the TPS, the utilization of inner phase shifts and the coexistence of different operation modes make the accurate switching average model complicated. In this paper, a simplified averaged model of the DAB is used as shown in Fig. 3.

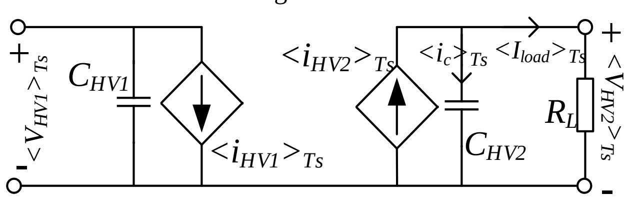

Fig. 3. The averaged model of the DAB.

The controlled current $<i_{HV2}>_{Ts}$ is calculated from equation (1). Substituting Table I into (1), the expressions for each operating mode are derived as in Table II.

$$< i_{HV2} >_{Ts} = \frac{1}{T_s}\int_0^{T_s} i_{HV2}\,dt \tag{1}$$

TABLE II
SWITCHING AVERAGED MODEL UNIFIED AT $V_{HV1}/(8f_sL_p)$

Mode	$<i_{HV2}>_{Ts}$
I	$\frac{32r_VD_f^2}{1-r_V}$
II	$\frac{-8(r_V^2+1)D_f^2+4(2r_V^2-r_V+1)D_f-(r_V-1)^2}{r_V^2}$
III	$\frac{32D_f^2}{r_V-1}$
IV	$-16(r_V^2-2r_V+2)D_f^2+8(r_V^2-2r_V+2)D_f-(r_V-1)^2$

The differential equation of the output voltage is developed from Fig. 3 as follows:

$$\frac{d<V_{HV2}>_{Ts}}{dt} = \frac{<i_{HV2}>_{Ts}}{C_{HV2}} - \frac{<V_{HV2}>_{Ts}}{R_LC_{HV2}} \tag{2}$$

The small signal models are derived by superimposing small perturbations on the equilibrium points. The control to output transfer functions for TPS-DAB are provided in Table III.

TABLE III
OPEN LOOP CONTROL TO OUTPUT TRANSFER FUNCTION

Mode	$G_{TPS}(s) = V_{HV2}(s)/D_f(s)$
I	$G_{TPS\_I}(s) = \frac{8\overline{D_f}\,\overline{V_{HV1}}\,\overline{r_V}R_L(1-\overline{r_V})}{C_{HV2}f_sL_pR_L(1-\overline{r_V})^2s-4R_L\overline{D_f}^2+f_sL_p(\overline{r_V}^2-\overline{r_V}+1)}$
II	$G_{TPS\_II}(s) = -\frac{2R_L\overline{V_{HV1}}\,\overline{r_V}(4\overline{D_f}+\overline{r_V}+4\overline{D_f}\,\overline{r_V}^2-2\overline{r_V}^2-1)}{4C_{HV2}f_sL_pR_L\overline{r_V}^3s-8R_L\overline{D_f}^2-2R_L\overline{D_f}\,\overline{r_V}+4R_L\overline{D_f}+4f_sL_p\overline{r_V}^3+R_L\overline{r_V}-R_L}$
III	$G_{TPS\_III}(s) = \frac{8\overline{D_f}\,\overline{V_{HV1}}R_L(\overline{r_V}-1)}{sC_{HV2}f_sL_pR_L(1-\overline{r_V})^2+4R_L\overline{D_f}^2+f_sL_p(1-\overline{r_V})^2}$
IV	$G_{TPS\_IV}(s) = \frac{-4R_L\overline{V_{HV1}}(4\overline{D_f}-1)(\overline{r_V}^2-2\overline{r_V}+2)}{4C_{HV2}f_sL_pR_Ls+4f_sL_p-R_L+R_L\overline{r_V}-16\overline{D_f}^2R_L+8\overline{D_f}R_L-8\overline{D_f}\,\overline{r_V}R_L+16\overline{D_f}^2\,\overline{r_V}R_L}$

, where the notation with a bar $\overline{X}$ denotes the equilibrium points.

In order to verify the correctness of the control to output transfer functions G_{TPS}(s) listed in Table III. Simulations have been conducted using the software PLECS block set 3.6.1 built in with MATLAB SIMULINK 2017a. The converter parameters are provided as in Table IV, otherwise specified.

Comparisons between the math models in Table III and the AC swept transfer functions $G_{TPS}(s)$ based on the ideal averaged model in Fig. 3 are carried out. The AC sweeping diagram with the ideal model is depicted in Fig. 4. Sinusoidal small perturbations are injected and superimposed on the equilibrium value of $\overline{D_f}$. Correspondent frequency components of the output voltage are measured. The open loop control to output transfer function can then be calculated as:

$$G_{TPS}(f) = \frac{V_{HV2}(f)}{D_f(f)} \tag{3}$$

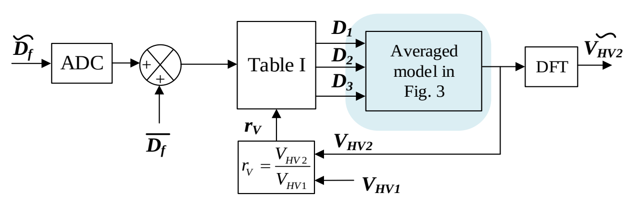

Fig. 4. Transfer function AC sweeping diagram with the averaged model.

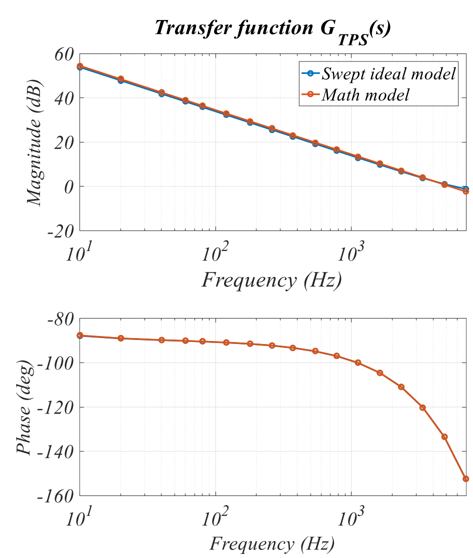

Fig. 5. Comparison between the AC swept ideal model and the math model in Table III under 260V/300V 10W Mode III.

The results are illustrated in Fig. 5. The math model agrees well with the swept ideal model. This confirms the correctness

This article has been accepted for publication in a future issue of this journal, but has not been fully edited. Content may change prior to final publication. Citation information: DOI 10.1109/TPEL.2019.2962838, IEEE Transactions on Power Electronics

of the math model in Table III. It is worth mentioning that the ideal model is a first order system. Ideally, the phase should be always negative 90 degree. However, as shown in Fig. 5 the phase is larger than negative 90 degree in low frequency due to the impact from R_L. The phase is smaller than negative 90 degree in high frequency due to the digital sampling delay reflected as $e^{-s/2fs}$ in multiplication to transfer functions from Table III.

C. The PI control for TPS-DAB

With the above developed transfer function in Table III, a PI voltage control with load current feedforward structure is utilized as a comparison benchmark. Sampling of the output voltage V_{HV2} and load current I_{load} are required. The PI voltage controller is defined as:

$$Gv(s) = K_p + \frac{K_i}{s} \tag{4}$$

The simplified control block diagram is depicted in Fig. 6. The transfer function $G_{TPS}(s)$ is variant with the operating terminal voltages and power. Moreover, due to the co-existence of four operating modes, the PI controller parameter design becomes overwhelming. In the following sections, PI parameters K_p and K_i defined in (4) are only designed and tuned at the points of interest for comparison purpose.

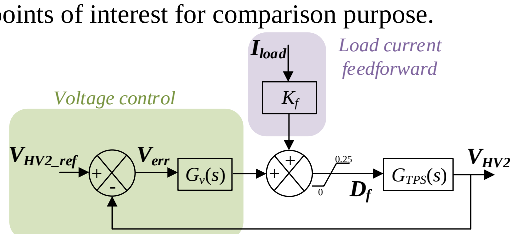

Fig. 6. The PI control block diagram

D. Remarks on the design issues with PI

When the TPS modulation is applied to DAB converters. The small signal model of the TPS-DAB is variant. It depends on the operating modes, terminal voltages and load power. In a single point of operation, the PI controller can be easily designed and tuned. However, when the converter operating condition is changed, the performance will be deteriorated. This phenomena will be addressed in the section III.B. Considering there are many operating modes in TPS-DAB, it is complex to optimally design the control parameters for TPS-DAB working in a wide terminal voltages and power range.

To address the above mentioned issue, this paper develops a controller for the TPS-DAB with the information of terminal voltages and circuit parameters embedded in the algorithm. The proposed controller presents better global dynamic performance with easier parameter tuning compared to the conventionally PI controller for TPS-DAB.

III. PROPOSED MDCS-MPC

The main objective of the control in the case of study is to regulate the bus voltage V_{HV2} supplying power to resistive loads. Based on the averaged model described in Fig. 3, the discretised difference equation of the output voltage is developed as follows:

$$V_{HV2}[k+1] = \frac{i_{HV2}[k+1] - I_{load}[k+1]}{C_{HV2}\, f_s} + V_{HV2}[k] \tag{5}$$

When the converter is loaded with the passive loads, the future load current is unknown. However, for a two-step prediction, the future load current is essential to predict voltage values of V_{HV2} at time instance k+2. Therefore, an assumption has been made that load current does not vary drastically in two sampling periods. This assumption has also been commonly used in MPC controlled inverters [27], [31].

$$I_{load}[k] = I_{load}[k+1] = I_{load}[k+2] \tag{6}$$

The prediction for output voltage at time instance k+2 is:

$$V_{HV2}[k+2] = \frac{i_{HV2}[k+2] - I_{load}[k]}{C_{HV2}\, f_s} + V_{HV2}[k+1] \tag{7}$$

Substituting (5) into (7), yields:

$$V_{HV2}[k+2] = \frac{i_{HV2}[k+2] + i_{HV2}[k+1] - 2I_{load}[k]}{C_{HV2}\, f_s} + V_{HV2}[k] \tag{8}$$

, where $i_{HV2}[k+1]$ and $i_{HV2}[k]$ can be easily derived from TABLE II.

In order to evaluate how realistic the assumption made in (6) is, and how accurate the prediction in (8) is, the prediction error has been defined in (9) as a metric.

$$V_e = \left| V_{HV2}[k+2] - V_{HV2\_s}[k+2] \right| \tag{9}$$

, where $V_{HV2\_s}[k+2]$ is the sampled load voltage at time instance k+2. A sinusoidal controlled current source is connected to the output terminal with a fixed amplitude but varying frequency. In (6), the load current is assumed to be constant within two sampling periods. Therefore, when load current changes slowly, this assumption is more likely to hold true. Results shown in Fig. 7 have verified this statement. When the load current has a frequency of 1kHz, the maximum prediction error is 0.293V. With the decreasing of the frequency down to 10Hz, the maximum prediction error is reduced to 0.008V. The error in the prediction will not necessarily cause problems. Since 1kHz is already above the bandwidth, 0.293V error is only 0.09% of rated voltage. Therefore, the assumption (6) has been deemed reasonable in our case of study.

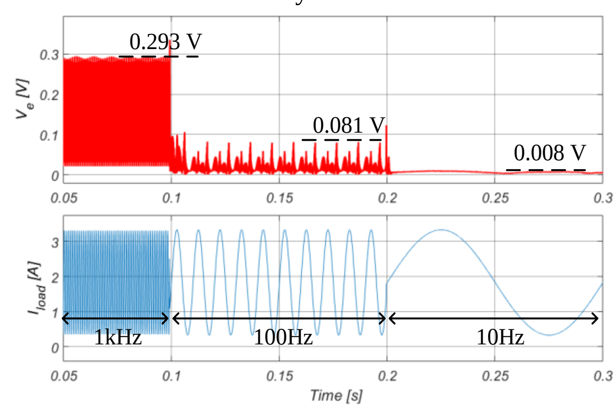

Fig. 7. Voltage prediction error evaluation.

A. The operating principle

The proposed MDCS-MPC controls the converter output voltage V_{HV2} based on the discretized average model of the DAB in Fig. 3. Taking into account the computational delay, MDCS-MPC has a prediction step of two sampling periods. A preliminary cost function is proposed as in (10) with the only purpose of regulating voltage V_{HV2} to reference V_{HV2_ref}. It is worth mentioning that (10) is not the finalized cost function, but a simple one meant to help illustrate the operating principle of the proposed MDCS-MPC.

$$ct = (V_{HV2\_ref} - V_{HV2}[k+2])^2 \tag{10}$$

It should be noted that according to TABLE I and II, there is only one control variable D_f rather than three. The variable D_f is continuous in nature. However, in digital control, D_f needs to be discretized. The discretization precision is subjected to the control platform applied. Δ_f is defined (11) as the finest phase shift value that can be achieved in a digital control platform as shown in Fig. 8.

$$\Delta_f = \frac{f_s}{f_c} \tag{11}$$

, where f_c is the peripheral clock frequency of the digital control platform. For unidirectional power flow, DAB works predominately in the range:

$$D_f \in [0, 0.25] \tag{12}$$

(12) is further discretized into μ_m (=0.25/Δ_f+1) elements as described in array (13).

$$D_f \in \{0, \Delta_f, 2\Delta_f, \cdots, 0.25\} \tag{13}$$

In order to implement a control algorithm that is feasible on standard commercial microcontrollers, the proposed MDCS-MPC evaluates a reduced number of values in each sampling period. In one sampling period, μ ($\mu \le \mu_m$) number of points are assessed. They are centered at the previous working point.

An intuitive illustration of the proposed MDCS-MPC is depicted in Fig. 9. In the control interval k to k+1, μ=3 points are evaluated centred at the previous working point $D_f[k] = a$. When $D_f[k+1]$ equals to a-Δ_f, a and a+Δ_f, the output voltage V_{HV2} is predicted as $V_{HV2}^{(1)}[k+2]$, $V_{HV2}^{(2)}[k+2]$ and $V_{HV2}^{(3)}[k+2]$. The superscript represents the index of an element in the moving discretized control set.

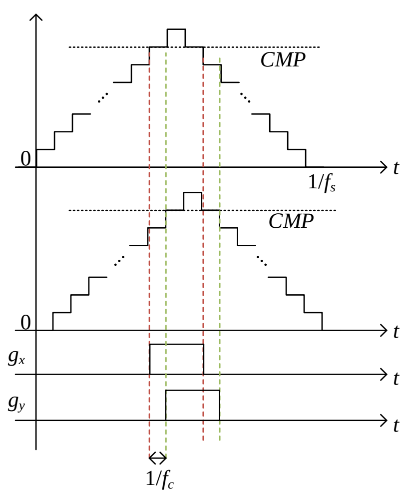

Fig. 8. Demonstration of the finest phase shift value in PWM modules.

The moving discretized control set during the period k to k+1 is $\{a-\Delta_f, a, a+\Delta_f\}$. According to the illustration in Fig. 9, when $D_f[k+1] = a+\Delta_f$, the predicted output voltage $V_{HV2}^{(3)}[k+2]$ is the closest to V_{HV2_ref}. This results in the smallest cost function defined in (10). Therefore, the value $a+\Delta_f$ is applied at time instance k+1 to D_f. In the next control interval, the same process is repeated. However, the moving discretized control set has changed. It has become $\{a, a+\Delta_f, a+2\Delta_f\}$. The control set is moving with the working point within the domain of (13). In this control interval, $D_f[k+3] = a$ results in the smallest cost function. Therefore, this value is applied at the time instance k+2. This process goes on.

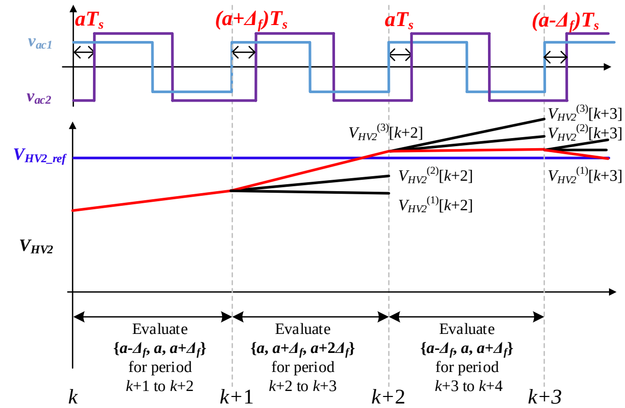

Fig. 9. The operating principle of the proposed MDCS-MPC for DAB. μ is set to be 3 for illustration.

Larger value of μ can increase the transition dynamics, but it aggravates the computational burden to the real-time digital controller. Therefore, an adaptive step for D_f is adopted instead of the finest search step Δ_f. Define the adaptive step Δ_{adp} as (15), (16). The adaptive step Δ_{adp} changes with the deviation of the output voltage to the reference. When V_{HV2} is far from the reference, Δ_{adp} grows large. In contrast, when V_{HV2} equals to the reference, Δ_{adp} becomes Δ_f. Such that, the control accuracy remains.

$$V_\Delta = \begin{cases} |V_{HV2\_ref} - V_{HV2}[k]|, & |V_{HV2\_ref} - V_{HV2}[k]| < V_m \\ V_m, & |V_{HV2\_ref} - V_{HV2}[k]| > V_m \end{cases} \tag{14}$$

$$\Delta_{adp} = \Delta_f (1 + \lambda V_\Delta^{\ 2}) \tag{15}$$

, where V_m is the saturated voltage. λ is a coefficient determined according to the requirement of transition performance. λ and V_m are set as 1, 10V respectively in the following simulation and experiment validations.

B. The proposed cost function

In order to help the system to converge, a second term G_2 is proposed in the cost function as follow:

$$ct = \alpha_1 G_1 + \alpha_2 G_2 \tag{16}$$

, where

$$\begin{cases} G_1 = (V_{HV2\_ref} - V_{HV2}[k+2])^2 \\ G_2 = (V_{HV2}[k+2] - V_{HV2}[k])^2 \end{cases} \tag{17}$$

The first term G_1 is responsible for regulation of the output voltage V_{HV2} to reference value V_{HV2_ref} while the second term G_2 takes charge of the system convergence. Fig. 10 shows how the weighting factor α_2 affects the convergence of bridge current $\langle i_{HV2} \rangle_{Ts}$ and load voltage V_{HV2}. The value of α_2 has a positive effect on the system convergence. When α_2 is zero, the system does not converge. However, α_2 cannot be set too large because it has negative impact on the control bandwidth. This will be addressed later in this section.

In order to provide a quantitative assessment on the performance of MDCS-MPC using the cost function in (16), the

This article has been accepted for publication in a future issue of this journal, but has not been fully edited. Content may change prior to final publication. Citation information: DOI 10.1109/TPEL.2019.2962838, IEEE Transactions on Power Electronics

frequency response is utilized. The small signal models of DAB converters are often carried out to analytically derive its frequency response. However, this is infeasible to describe the DAB converters with non-linear controllers. Another approach is utilized here. If a certain small sinusoidal perturbation signal that is applied to a nonlinear element always excites a sinusoid at the same frequency in the output, then such an element can be represented by its linear "equivalent" frequency response, which is commonly called a describing function ([32], ch.5). As a result, standard frequency domain techniques can be used to assess the characteristics of the converter which comprises nonlinear elements [27]. The same as the analytical method (small signal modelling), the describing function method also needs to have its assessments carried out based on a given equilibrium point. Small signal perturbations have been injected to the converter and responses have been measured with the correspondent frequency. This numerical method applies to both linear and non-linear controls.

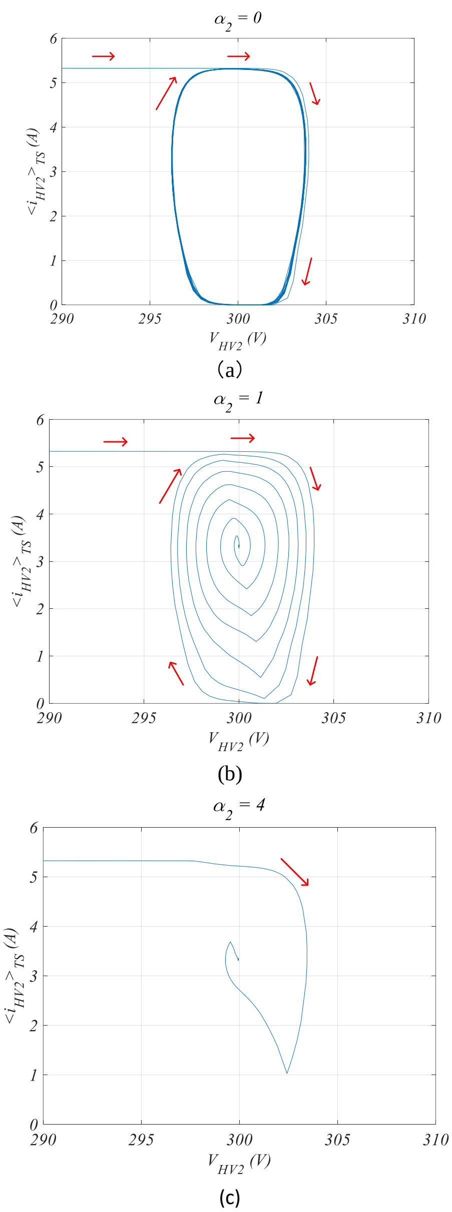

Fig. 10. Phase portrait with different α_2

The AC sweepings are carried out in the switching model under the equilibrium point 260V/300V 1kW. Perturbations from 10Hz to 10kHz with amplitude of 0.01V are superimposed on the output voltage equilibrium value V_{HV2_ref}=300V as shown in Fig. 11. The close loop transfer function is defined as in (18).

$$G_{R2O}(f) = \frac{V_{HV2}(f)}{v^{*}_{HV2}(f)} \tag{18}$$

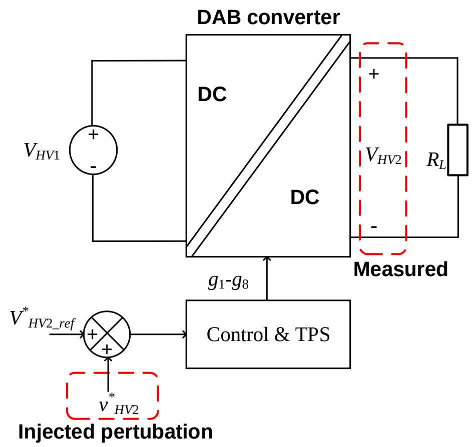

Fig. 11. Frequency response sweeping circuit.

The results are presented in Fig. 12. In the figure, the close loop transfer functions in the frequency domain with different values of α_2 and μ are shown. In observation of the solid lines (α_2=1), μ increases the amplitude of $G_{R2O}(f)$ in the high frequency range. When comparing lines with round markers (μ=3), it can be concluded that α_2 has a negative impact to the amplitude of $G_{R2O}(f)$ in the low to medium frequency range. Parameters α_2 and μ have clear implications on $G_{R2O}(f)$. The PI parameters are designed based on the ideal/math model under the equilibrium point 260V/300V 1kW. The control parameters are designed as K_p=0.05, K_i=10. The gain and phase margins are 15.4dB and 72deg, respectively. The crossover frequency is 570Hz. As shown in the figure, the frequency response line of PI sits between the blue and red lines of MDCS-MPC. If tuned with α_2=1 and a μ between 3 and 11, the MDCS-MPC can present very similar frequency response as the designed PI.

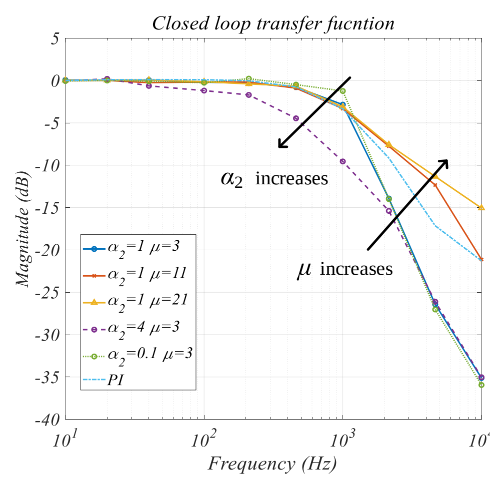

Fig. 12. Sweeping results for $G_{R2O}(f)$ in (18) under equilibrium point 260V/300V 1kW

This article has been accepted for publication in a future issue of this journal, but has not been fully edited. Content may change prior to final publication. Citation information: DOI 10.1109/TPEL.2019.2962838, IEEE Transactions on Power Electronics

In order to guarantee the performance, the control parameters of the PI controller have to be designed based on a single equilibrium point. When the operating point varies, $G_{R2O}(f)$ will change as well. For example, as shown in Fig. 13, with the PI controller, when the input voltage V_{HV1} reduces from 260V (yellow line) to 180V (purple line), the amplitude of $G_{R2O}(f)$ varies significantly. In comparison, when MDCS-MPC is used, $G_{R2O}(f)$ can largely maintain. The above mentioned phenomena about PI controller and MDCS-MPC can also be confirmed in experiments Fig. 21 and Fig. 22.

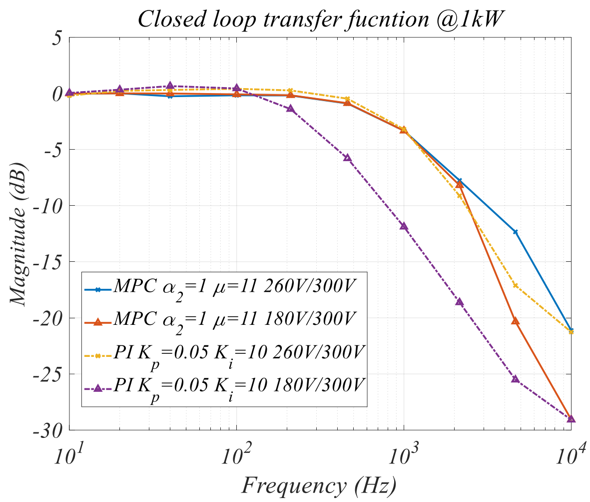

Fig. 13. Frequency response with different input voltage.

The reference tracking performance of the PI and the proposed method in the time domain has also been compared. As shown in Fig. 14, the load voltage reference changes between 300V and 260V. At time instance t_1, when the proposed control is used, D_3 starts to increase 0.55ms before V_{HV2} reaches the reference 260V. In contrast, when PI is used, D_3 can only start to increase once V_{HV2} reaches 260V. The similar phenomena can also be observed at time instance t_3 and t_4. The feature ensures MDCS-MPC to provide better voltage tracking performance. This phenomena is also confirmed in experiment Fig. 25 and Fig. 26.

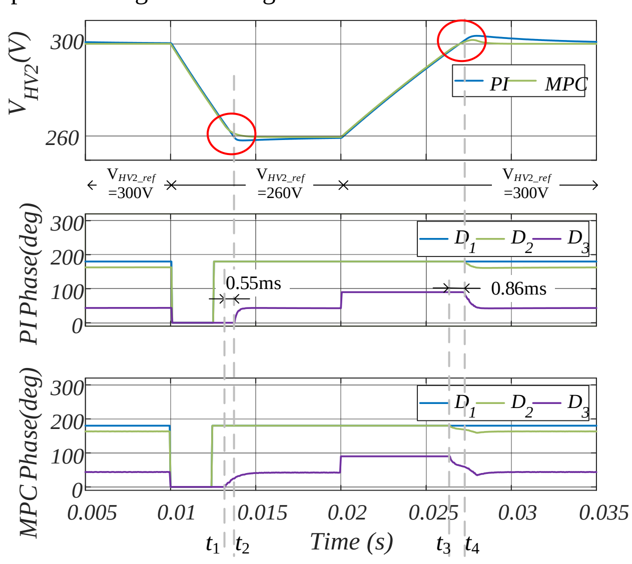

Fig. 14. Load voltage reference tracking.

C. Flexible multi-objective control

The proposed MDCS-MPC can be extended to applications where multi-objective control is required. Control objectives can be coordinately achieved by adding terms in the cost function as with FCS-MPC [27].

In order to demonstrate this benefit, apart from the regulation of the output voltage V_{HV2}, the DAB is assigned also another task to stabilize the input voltage V_{HV1} in presence of oscillation due to the well-known constant power load stability issue [33]. A DAB converter with an input LC filter is illustrated in Fig. 15 to showcase the scenario.

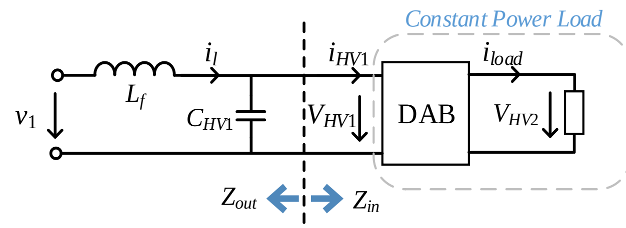

Fig. 15. DAB with an input LC filter.

Instability could happen when Z_{out}/Z_{in} does not satisfy the impedance based Nyquist stability criterion [34]. Therefore, stabilization control is required. The cost function is then proposed as:

$$ct = \alpha_1 G_1 + \alpha_2 G_2 + \alpha_3 G_3 \tag{19}$$

, where

$$G_3 = (V_{HV1}[k+2] - v_1[k])^2 \tag{20}$$

$$V_{HV1}[k+2] = \frac{2I_{load}[k] - (i_{HV1}[k+2] + i_{HV1}[k+1])}{C_{HV2}\, f_s} + V_{HV1}[k] \tag{21}$$

The only difference between the calculation of the current i_{HV1} and i_{HV2} is that i_{HV1} is unified at $V_{HV2}/(8f_sL_p)$ while i_{HV2} is unified at $V_{HV1}/(8f_sL_p)$ in Table II.

The effectiveness of the stabilization term G_3 has been verified in the experiment Section V.C. Since this paper focuses only on the proposal of the MDCS-MPC idea in TPS-DAB, and scenario in Fig. 15 is only used to showcase the capability of MDCS-MPC. Further detailed analysis on system stabilization is not discussed.

IV. Steady State Error Analysis

Two causes for the steady state error specifically in the proposed MDCS-MPC are addressed in this section. Relevant error compensation approaches are elaborated.

The first cause is the prediction error from the ideal model. As stated earlier in the Section II, the accurate modeling of the DAB modulated with TPS is rather complicated. The simplified reduced order model in Fig. 3 enables relatively easier implementation, however, it also brings perdition error in $\langle i_{HV2} \rangle_{Ts}$.

The second cause is the contradiction between G_1 and G_2. When V_{HV2} reaches close to V_{HV2_ref}, G_1 becomes very small. The predicted step change ($V_{HV2}[k+2]$-V_{HV2}[k]) is higher than the steady state error (V_{HV2_ref}-$V_{HV2}[k+2]$). In this case, the decreasing of $\alpha_1 G_1$ does not compensate for the increasing of $\alpha_2 G_2$. (V_{HV2_ref}-$V_{HV2}[k+2]$) cannot be zero therefore causing the steady state error..

This article has been accepted for publication in a future issue of this journal, but has not been fully edited. Content may change prior to final publication. Citation information: DOI 10.1109/TPEL.2019.2962838, IEEE Transactions on Power Electronics

A. Error caused by the prediction model

The error of the ideal prediction model in TABLE II can be corrected by a compensation term defined as I_{comp} in (22). I_{comp} is calculated as the difference between the observed output current value i_{HV2_r} and the predicted value i_{HV2}.

$$I_{comp}[k] = i_{HV2\_r}[k-1] - i_{HV2}[k-1] \tag{22}$$

, where

$$i_{HV2\_r}[k-1] = \frac{C_{HV2}}{T_s}(V_{HV2}[k] - V_{HV2}[k-1]) + I_{load}[k-1] \tag{23}$$

The correction of the prediction model can eliminate the steady state error for the output voltage. However, due to the calculation of i_{HV2_r} in (23) involves derivative of V_{HV2}. In presence of sampling noise, the compensation term I_{comp} could deteriorate the dynamic performance of MDCS-MPC. I_{comp} is designed solely for the purpose of steady state error correction. A Low Pass Filter (LPF) can be applied for I_{comp}. Therefore, the predicted output voltage is modified as in (24). A diagram of the compensation for the prediction error is shown in Fig. 16. A moving average filter is used as the LPF. The effectiveness of the prediction error compensation is verified by both simulations and experiments in Section V and VI.

$$V_{HV2}[k+2] = \frac{i_{HV2}[k+2] + i_{HV2}[k+1] + 2I_{comp\_f}[k] - 2I_{load}[k]}{C_{HV2} f_s} + V_{HV2}[k] \tag{24}$$

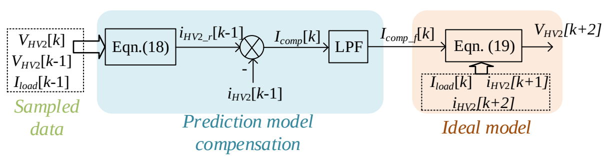

Fig. 16. The compensation diagram for the prediction error

B. Error caused by the weighting factor α_2

In this subsection, the steady state error caused by the weighting factor α_2 is analyzed. To start with, consider the initial cost function in (10) without G_2 and assume, the converter has already been in the steady state:

$$V_{HV2}[k] = V_{HV2}[k+1] \tag{25}$$

$$I_{load}[k] = i_{HV2}[k] = i_{HV2}[k+1] \tag{26}$$

, where the steady state error V_{err_org} is defined as:

$$V_{err\_org} = V_{HV2\_ref} - V_{HV2}[k] \tag{27}$$

Substitute the condition (26) and (27) into the prediction model (8). The prediction value for the output voltage $V_{HV2}^{(3)}[k+1]$ in Fig. 17 is:

$$V_{HV2}[k+2] = \frac{i_{HV2}[k+2] - i_{HV2}[k+1]}{C_{HV2} f_s} + V_{HV2\_ref} - V_{err\_org} \tag{28}$$

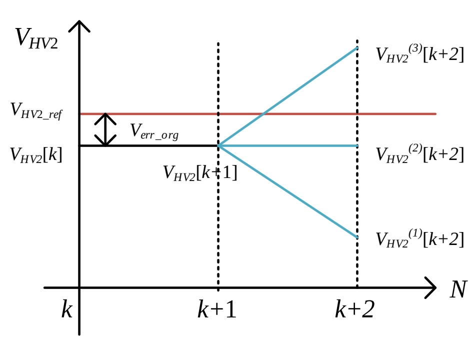

Fig. 17. Illustration of the steady state error

Equation (28) can be further modified as:

$$V_{HV2}[k+2] = \frac{\Delta_{adp}}{C_{HV2} f_s}\frac{di_{HV2}}{dD_f}\Big|_{Df=\overline{Df}} + V_{HV2\_ref} - V_{err\_org} \tag{29}$$

The cost functions with voltage predictions $V_{HV2}^{(2)}[k+2]$ and $V_{HV2}^{(3)}[k+2]$ are:

$$ct^{(2)} = V_{err\_org}^{\ 2} \tag{30}$$

$$ct^{(3)} = \left(\frac{\Delta_{adp}}{C_{HV2} f_s}\frac{di_{HV2}}{dD_f}\Big|_{Df=\overline{Df}} - V_{err\_org}\right)^2 \tag{31}$$

Due to the steady state assumption, (32) has to hold true.

$$ct^{(2)} < ct^{(3)} \tag{32}$$

Therefore, the maximum prediction error $V_{err\_org\_max}$ can be obtained in (33).

$$V_{err\_org} < \frac{\Delta_{adp}}{C_{HV2} f_s}\frac{di_{HV2}}{dD_f}\Big|_{Df=\overline{Df}} = V_{err\_org\_\max} \tag{33}$$

Now, consider the cost function defined in (16) with the second term G_2 enabled. Set α_1=1. The cost functions with the voltage prediction $V_{HV2}^{(2)}[k+2]$ and $V_{HV2}^{(3)}[k+2]$ become:

$$ct^{(2)} = V_{err\_\mathrm{mod}}^{\ 2} \tag{34}$$

$$ct^{(3)} = \left(\frac{\Delta_{adp}}{C_{HV2} f_s}\frac{di_{HV2}}{dD_f}\Big|_{Df=\overline{Df}} - V_{err\_\mathrm{mod}}\right)^2 + \alpha_2\left(\frac{\Delta_{adp}}{C_{HV2} f_s}\frac{di_{HV2}}{dD_f}\Big|_{Df=\overline{Df}}\right)^2 \tag{35}$$

, where V_{err_mod} is the steady state error with the term G_2 enabled.

Due to the steady state assumption, substitute (33), (34) and (35) in (32). The maximum prediction error $V_{err\_mod\_max}$ becomes:

$$V_{err\_\mathrm{mod}} < V_{err\_org\_\max}(1+\alpha_2) = V_{err\_\mathrm{mod}\_\max} \tag{36}$$

The steady state error is dependent on the working points of the converter such as power and the terminal voltage ratio. Conclusion can be drawn from (33) that smaller step Δ_{adp}, bigger output capacitor C_{HV2} and higher switching frequency f_s are conducive for the reduction on the voltage steady state error. It also can be concluded from (36) that the existence of α_2 increases the original steady state error $V_{err\_org\_max}$ with only G_1 in the cost function by a multiplier of (1+ α_2). Higher values of α_2 introduces higher attenuation to sampling noise and damping effect, however, it may slow down the dynamic and cause larger steady state output voltage error.

In applications typically with large output capacitor and high switching frequency, the error is small enough to be neglected. However, in some cases where high voltage precision is required, the adaptive weighting factor design proposed by *T. Dragicevic* [35] can be adopted to address the issue.

V. EXPERIMENTAL RESULTS

The proposed methodology has been validated on a 1kW 20kHz laboratory prototype. The load R_L is switched on and off by a solid-state circuit breaker (SSCB). Bench power supply EA-PS 9360-40 3U (1 Output, 0 V-360 V, 0 A-40 A) is connected directly to the DAB providing stiff input voltage V_{HV1}. The experiment prototype is shown in Fig. 18. A TMS320F2837xD evaluation board from Texas Instruments has been adopted as the digital control platform which communicates with a host computer. IGBT device SKM75GB128D is used as full bridge switches with 1.6us software dead time. Two 380uF 400V polypropylene capacitors from KEMET are utilized for each DC terminal. The integrated

This article has been accepted for publication in a future issue of this journal, but has not been fully edited. Content may change prior to final publication. Citation information: DOI 10.1109/TPEL.2019.2962838, IEEE Transactions on Power Electronics

transformer and inductor (Lp=300uH) are made by MnZn ferrites with 3.9mm^2 litzs wire. The magnetizing inductance is L_m=3mH. Circuit and control parameters in Table IV are used in the experiment, otherwise specified. The main components used in the prototype are summarized in Table V.

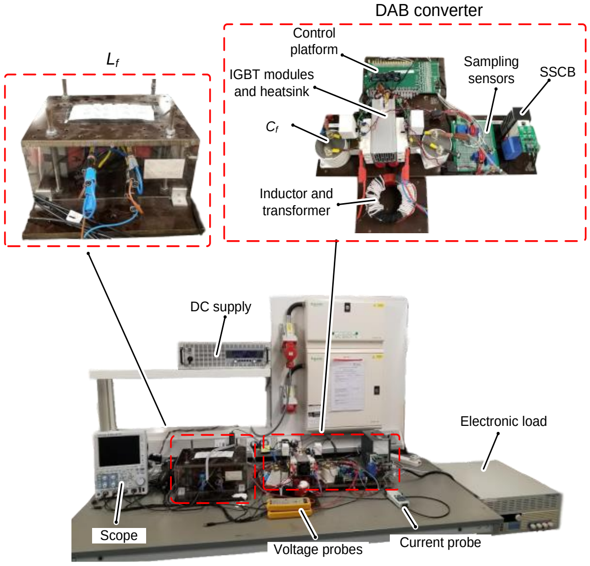

Fig. 18. The experiment setup.

TABLE IV
CIRCUIT & CONTROL PARAMETERS

Description	Value	Units
Switching frequency f_s	20	kHz
Dead time t_d	1.6	µS
Transformer turn ratio	20:20	/
Primary power inductor L_p	300	µH
Parasitic resistance R_p	50	mΩ
Primary DC capacitor C_{HV1}	380	µF
Secondary DC capacitor C_{HV2}	380	µF
Rated power	1	kW
Adaptive step saturate V_m	10	V
Adaptive step factor λ	1	/
Searching points μ	11	/
Weighting factor α_1	1	/
Weighting factor α_2	4	/
Proportional coefficient K_p	0.05	/
Integral coefficient K_i	3.57	/
Feedforward coefficient K_f	0.01	/

TABLE V
HARDWARE COMPONENTS

Component	**Description**	**Parameters**
Switching devices	SKM75GB128D	V_{CES}=1200V; I_c=100A
Pri/Sec capacitors	C4DEFPQ6380A8TK, Polypropylene	380uF; 400V
Magnetic components	MnZn Ferrites; 3.9mm^2 litz wire	L_m=3mH; L_p=0.3mH
Voltage sensors	LV 25-P	t_r=40us
Current sensors	LA 55-p	BW(-1dB) 200kHz

A. Steady state error compensation of MDCS-MPC

The effectiveness of the steady state error compensation loop proposed in Fig. 16 is verified in this subsection. Experiments are carried out under the condition: 300V input voltage V_{HV1} and 300V output voltage reference V_{HV2_ref}. Waveforms of the MDCS-MPC without the compensation are captured in presence of load variation @20Hz as in Fig. 19. Except for the existence of the steady state error, without compensation, the proposed MDCS-MPC demonstrates superior load disturbance rejection ability in the experiment. There is no oscillation in both transition and steady state. It is clear that there is a difference between the steady state values when changing the load power. When the compensation loop is enabled, the steady error can be much smaller compared to the results without compensations. Fig. 20 shows the steady state measurement results of the output voltage mean value.

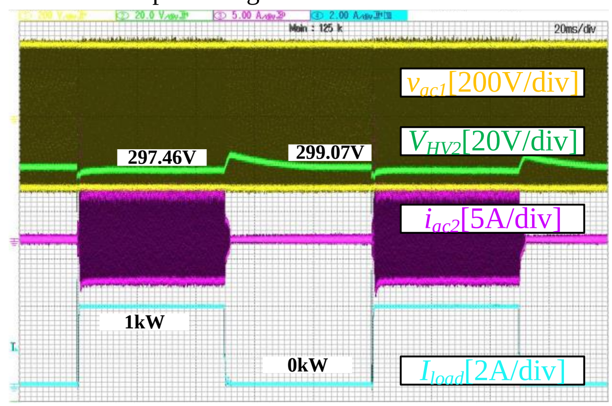

Fig. 19. MDCS-MPC controlled DAB loaded with load variations @20Hz. Prediction compensation disabled. V_{HV1}=300V, V_{HV2_ref}=300V.

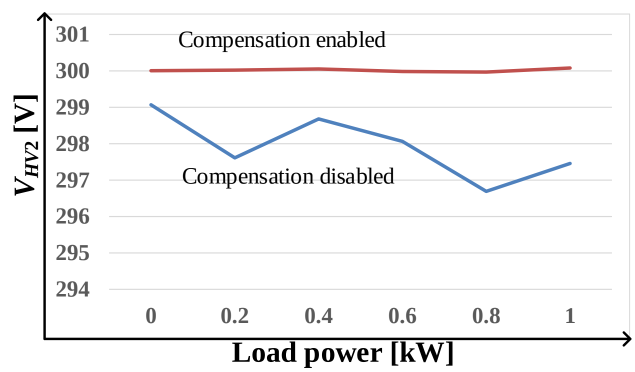

Fig. 20. Compensation for the prediction error as illustrated in Fig. 16. Operation under V_{HV1}=300V, V_{HV2_ref}=300V over the whole power range.

B. Performance comparisons

The experiment results with load step up/down are provided in Fig. 21 and Fig. 22. In Fig. 21, the input voltage is set 300V, output voltage reference is set 300V. The load power jumps between 1kW and 210W at a frequency of 20Hz. In Fig. 22, the input voltage is reduced to 260V. When compared with Fig. 21, the performance of TPS-DAB is deteriorated with PI controller. This confirms the assessment in Fig. 13. In contrast, when MDCS-MPC is used, the performance remains well even when terminal voltage is changed. The MDCS-MPC has good performance throughout the voltage and power range. The steady state waveforms of Fig. 21 and Fig. 22 are presented in Fig. 23 and Fig. 24.

This article has been accepted for publication in a future issue of this journal, but has not been fully edited. Content may change prior to final publication. Citation information: DOI 10.1109/TPEL.2019.2962838, IEEE Transactions on Power Electronics

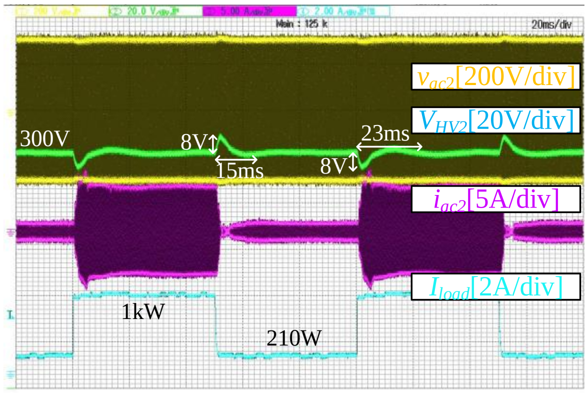

(a) PI controller

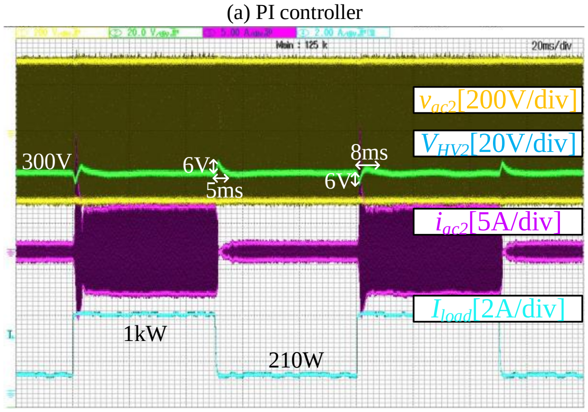

(b) MDCS-MPC

Fig. 21. Transition waveforms under V_{HV1}=300V, V_{HV2_ref}=300V

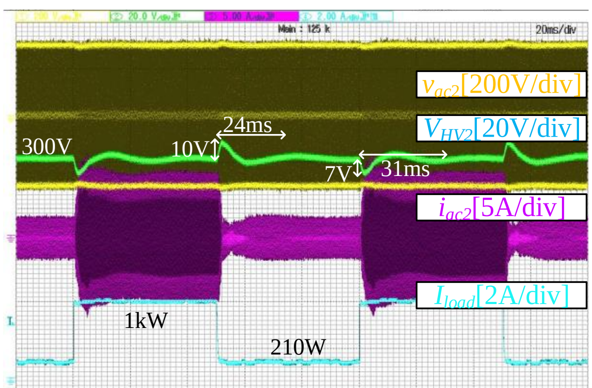

(a) PI controller

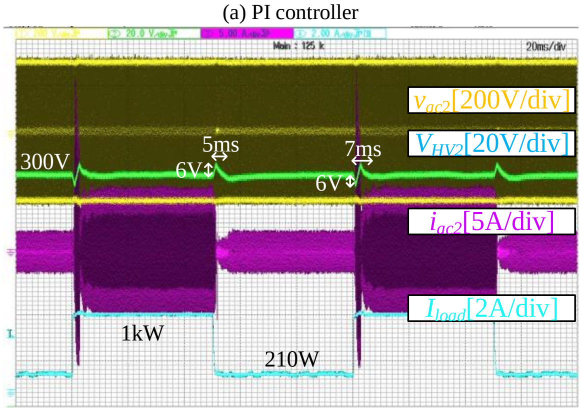

(b) MDCS-MPC

Fig. 22. Transition waveforms under V_{HV1}=260V, V_{HV2_ref}=300V

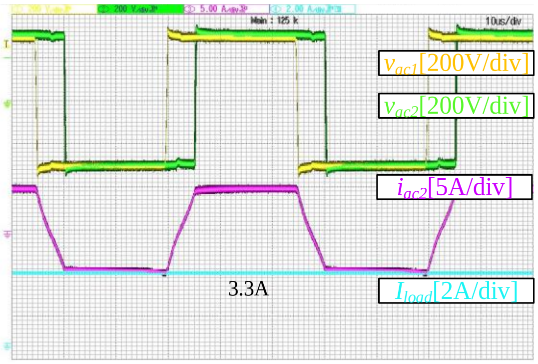

(a) 1kW

(b) 210W

Fig. 23. Steady state waveform under 300V/300V

(a) 1kW

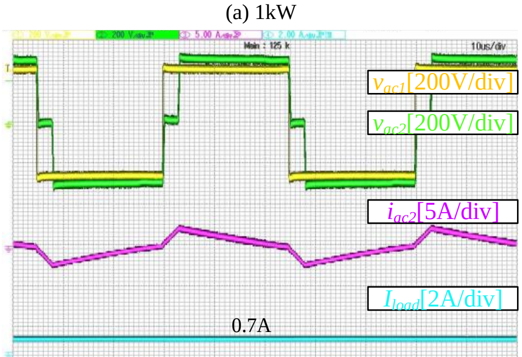

(b) 210W

Fig. 24. Steady state waveform under 260V/300V

Experiments on the step change of the reference voltage are also conducted. The output voltage reference are changed between 260V and 300V. The transition results are presented in Fig. 25 and Fig. 26. In the experiment with MDCS-MPC, the voltage overshoot/dig is very small, thus ending in fast voltage tracking compared to the PI controller. The results again

This article has been accepted for publication in a future issue of this journal, but has not been fully edited. Content may change prior to final publication. Citation information: DOI 10.1109/TPEL.2019.2962838, IEEE Transactions on Power Electronics

confirm the superior performance of the proposed MDCS-MPC in the regulation over the voltage reference.

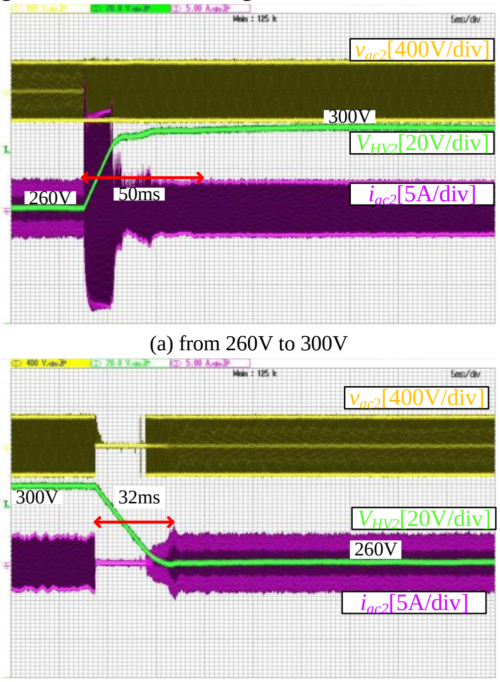

(a) from 260V to 300V

(b) from 300V to 260V

Fig. 25. Change of voltage reference V_{HV2_ref} with MDCS-MPC

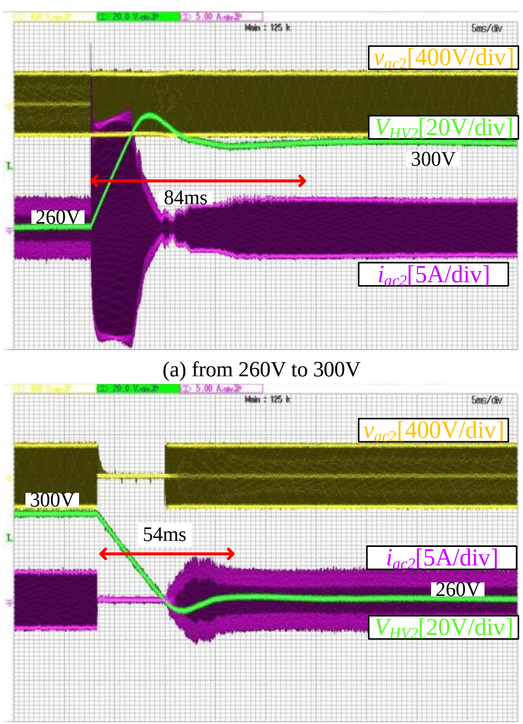

(a) from 260V to 300V

(b) from 300V to 260V

Fig. 26. Change of voltage reference V_{HV2_ref} with PI controller

C. Multi-objective control

Another advantage of the proposed MDCS-MPC is the multi-objective control capability. The experiment circuit is configured as Fig. 15 to demonstrate the performance. The DAB converter is responsible for both output voltage regulation and input voltage stabilization. The cost function proposed in (19) is used. The value of L_f is 11mH. The output capacitor C_{HV2} is reduced to 150uF. The experiment result is shown in Fig. 27. The converter starts operating with G_3 disabled. The input voltage V_{HV1} oscillates due to the impedance instability [34]. The output voltage V_{HV2} is not affected. It is still tightly regulated at 270V. At the time instance t_1, the stabilization term G_3 is enabled. The input voltage gets quickly stabilized. During the period t_1-t_2, the regulation of V_{HV2} is inevitably affected, however, both control objectives have been coordinately achieved at t_2.

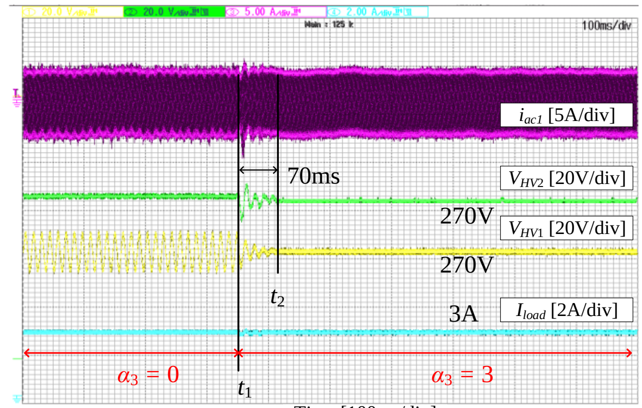

Fig. 27. Multi-objective control on both terminal voltages.

D. Computational time

The computational time of the proposed MDCS-MPC is evaluated as shown in Fig. 28. The PI controller takes 4.2us to run while, in contrast, the time to run MDCS-MPC varies with μ. In the experiment, μ=11 has already demonstrated good performance against PI controller, and it only takes 18.6us. Since 20 kHz switching frequency is utilized, 50us is available in one sampling period. Therefore, there is sufficient headroom for implementing A/D sampling, digital filters, MODBUS communication, protections etc.

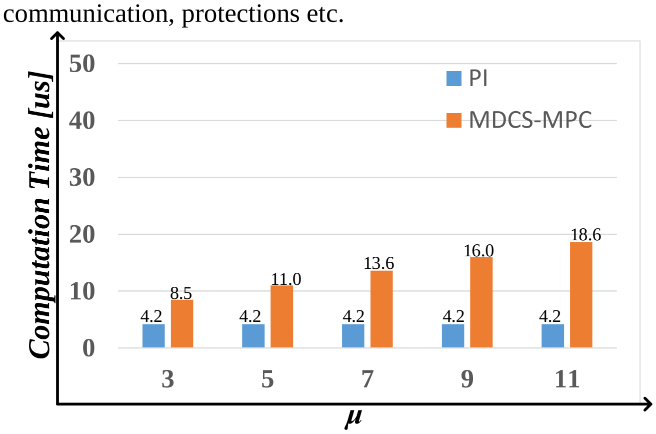

Fig. 28. Measurement of computational time.

VI. CONCLUSION

In this paper, a Moving-Discretized-Control-Set Model-Predictive-Control (MDCS-MPC) is proposed to TPS-DAB. Compared to conventional PI control, MDCS-MPC provides benefits as:

1, the MDCS-MPC presents good performance throughout wide voltage and power range. It utilizes global control parameters, which eases the design.

This article has been accepted for publication in a future issue of this journal, but has not been fully edited. Content may change prior to final publication. Citation information: DOI 10.1109/TPEL.2019.2962838, IEEE Transactions on Power Electronics

2, the flexibility of the finite control set - model predictive control has been enabled by MDCS-MPC in TPS-DAB. Multi-objective control can be easily achieved.

3, it is feasible to implement the MDCS-MPC on commercial control platforms due to the use of a small prediction horizon.

The performance of the proposed MDCS-MPC and PI is compared in the experiment with TPS-DAB. Theoretical claims have been confirmed.

REFERENCES

[1] K. W. Hu and C. M. Liaw, "Incorporated operation control of DC microgrid and electric vehicle," *IEEE Trans. Ind. Electron.*, vol. 63, no. 1, pp. 202–215, Jan. 2016.

[2] X. Zhaoxia, Z. Tianli, L. Huaimin, J. M. Guerrero, C.-L. Su, and J. C. Vasquez, "Coordinated Control of a Hybrid-Electric-Ferry Shipboard Microgrid," *IEEE Trans. Transp. Electrif.*, vol. 5, no. 3, pp. 828–839, Jul. 2019.

[3] S. Guenter *et al.*, "Load Control for the DC Electrical Power Distribution System of the More Electric Aircraft," *IEEE Trans. Power Electron.*, pp. 1–1, 2018.

[4] L. Chen, L. Tarisciotti, A. Costabeber, F. Gao, P. Wheeler, and P. Zanchetta, "Advanced modulations for a current-fed isolated DC-DC converter with wide voltage operating ranges," *IEEE J. Emerg. Sel. Top. Power Electron.*, pp. 1–1, 2018.

[5] Y. Shi, R. Li, Y. Xue, and H. Li, "Optimized Operation of Current-Fed Dual Active Bridge DC-DC Converter for PV Applications," *IEEE Trans. Ind. Electron.*, vol. 62, no. 11, pp. 6986–6995, Nov. 2015.

[6] Y. W. Cho, W. J. Cha, J. M. Kwon, and B. H. Kwon, "High-Efficiency Bidirectional DAB Inverter Using a Novel Hybrid Modulation for Stand-Alone Power Generating System with Low Input Voltage," *IEEE Trans. Power Electron.*, vol. 31, no. 6, pp. 4138–4147, Jun. 2016.

[7] Q. Ye, R. Mo, and H. Li, "Stability analysis and improvement of a dual active bridge (DAB) converter enabled DC microgrid based on a reduced-order low frequency model," in *2016 IEEE Energy Conversion Congress and Exposition (ECCE)*, 2016, pp. 1–7.

[8] Q. Ye, Ran Mo, and H. Li, "Impedance modeling and verification of a dual active bridge (DAB) DC/DC converter enabled DC microgrid in FREEDM system," in *2016 IEEE 8th International Power Electronics and Motion Control Conference (IPEMC-ECCE Asia)*, 2016, pp. 2875–2879.

[9] A. R. Alonso, J. Sebastian, D. G. Lamar, M. M. Hernando, and A. Vazquez, "An overall study of a Dual Active Bridge for bidirectional DC/DC conversion," *2010 IEEE Energy Conversion Congress and Exposition*. pp. 1129–1135, 2010.

[10] H. Bai, C. C. Mi, and S. Gargies, "The Short-Time-Scale Transient Processes in High-Voltage and High-Power Isolated Bidirectional DC-DC Converters," *IEEE Transactions on Power Electronics*, vol. 23, no. 6. pp. 2648–2656, 2008.

[11] C. Mi, H. Bai, C. Wang, and S. Gargies, "Operation, design and control of dual H-bridge-based isolated bidirectional DC-DC converter," *IET Power Electron.*, vol. 1, no. 4, pp. 507–517, 2008.

[12] B. Farhangi and H. A. Toliyat, "Piecewise Linear Model for Snubberless Dual Active Bridge Commutation," *IEEE Trans. Ind. Appl.*, vol. 51, no. 5, pp. 4072–4078, Sep. 2015.

[13] S. Shao, H. Chen, X. Wu, J. Zhang, and K. Sheng, "Circulating Current and ZVS-on of a Dual Active Bridge DC-DC Converter: A Review," *IEEE Access*, vol. 7, pp. 50561–50572, 2019.

[14] B. Zhao, Q. Yu, and W. Sun, "Extended-phase-shift control of isolated bidirectional DC-DC converter for power distribution in microgrid," *IEEE Trans. Power Electron.*, vol. 27, no. 11, pp. 4667–4680, 2012.

[15] B. Zhao, Q. Song, and W. Liu, "Efficiency characterization and optimization of isolated bidirectional DC-DC converter based on dual-phase-shift control for DC distribution application," *IEEE Trans. Power Electron.*, vol. 28, no. 4, pp. 1711–1727, Apr. 2013.

[16] S. Shao, M. Jiang, W. Ye, Y. Li, J. Zhang, and K. Sheng, "Optimal Phase Shift Control to Minimize Reactive Power for a Dual Active Bridge DC-DC Converter," *IEEE Trans. Power Electron.*, pp. 1–1, 2019.

[17] P. Karamanakos, T. Geyer, and S. Manias, "Direct Voltage Control of DC–DC Boost Converters Using Enumeration-Based Model Predictive Control," *IEEE Trans. Power Electron.*, vol. 29, no. 2, pp. 968–978, Feb. 2014.

[18] B. Wang, V. R. K. Kanamarlapudi, L. Xian, X. Peng, K. T. Tan, and P. L. So, "Model Predictive Voltage Control for Single-Inductor Multiple-Output DC–DC Converter With Reduced Cross Regulation," *IEEE Trans. Ind. Electron.*, vol. 63, no. 7, pp. 4187–4197, Jul. 2016.

[19] F. M. Oettmeier, J. Neely, S. Pekarek, R. DeCarlo, and K. Uthaichana, "MPC of Switching in a Boost Converter Using a Hybrid State Model With a Sliding Mode Observer," *IEEE Trans. Ind. Electron.*, vol. 56, no. 9, pp. 3453–3466, Sep. 2009.

[20] S. Dutta, S. Hazra, and S. Bhattacharya, "A Digital Predictive Current-Mode Controller for a Single-Phase High-Frequency Transformer-Isolated Dual-Active Bridge DC-to-DC Converter," *IEEE Trans. Ind. Electron.*, vol. 63, no. 9, pp. 5943–5952, Sep. 2016.

[21] Z. Shan, J. Jatskevich, H. H.-C. C. Iu, and T. Fernando, "Simplified Load-Feedforward Control Design for Dual-Active-Bridge Converters With Current-Mode Modulation," *IEEE J. Emerg. Sel. Top. Power Electron.*, vol. 6, no. 4, pp. 2073–2085, Dec. 2018.

[22] J. Huang, Y. Wang, Z. Li, and W. Lei, "Unified Triple-Phase-Shift Control to Minimize Current Stress and Achieve Full Soft-Switching of Isolated Bidirectional DC-DC Converter," *IEEE Trans. Ind. Electron.*, vol. 63, no. 7, 2016.

[23] K. Wu, C. W. de Silva, and W. G. Dunford, "Stability Analysis of Isolated Bidirectional Dual Active Full-Bridge DC–DC Converter With Triple Phase-Shift Control," *IEEE Trans. Power Electron.*, vol. 27, no. 4, pp. 2007–2017, Apr. 2012.

[24] T. Dragicevic, "Model Predictive Control of Power Converters for Robust and Fast Operation of AC Microgrids," *IEEE Trans. Power Electron.*, vol. 33, no. 7, pp. 6304–6317, Jul. 2018.

[25] L. Tarisciotti *et al.*, "Model Predictive Control for Shunt Active Filters With Fixed Switching Frequency," *IEEE Trans. Ind. Appl.*, vol. 53, no. 1, pp. 296–304, Jan. 2017.

[26] L. Tarisciotti, P. Zanchetta, A. Watson, S. Bifaretti, and J. C. Clare, "Modulated Model Predictive Control for a Seven-Level Cascaded H-Bridge Back-to-Back Converter," *IEEE Trans. Ind. Electron.*, vol. 61, no. 10, pp. 5375–5383, Oct. 2014.

[27] T. Dragicevic, "Dynamic Stabilization of DC Microgrids with Predictive Control of Point of Load Converters," *IEEE Trans. Power Electron.*, pp. 1–1, 2018.

[28] N. Hou, W. Song, and M. Wu, "Minimum-Current-Stress Scheme of Dual Active Bridge DC-DC Converter with Unified Phase-Shift Control," *IEEE Trans. Power Electron.*, vol. 31, no. 12, 2016.

[29] A. Tong, L. Hang, G. Li, X. Jiang, and S. Gao, "Modeling and Analysis of a Dual-Active-Bridge-Isolated Bidirectional DC/DC Converter to Minimize RMS Current with Whole Operating Range," *IEEE Trans. Power Electron.*, vol. 33, no. 6, pp. 5302–5316, Jun. 2018.

[30] K. Zhang, Z. Shan, and J. Jatskevich, "Large- and Small-Signal Average-Value Modeling of Dual-Active-Bridge DC–DC Converter Considering Power Losses," *IEEE Trans. Power Electron.*, vol. 32, no. 3, pp. 1964–1974, Mar. 2017.

[31] S. Kouro, P. Cortés, R. Vargas, U. Ammann, and J. Rodríguez, "Model predictive control—A simple and powerful method to control power converters," *IEEE Trans. Ind. Electron.*, vol. 56, no. 6, pp. 1826–1838, 2009.

[32] J. Slotine and W. Li, *Applied Nonlinear Control*, Vol. 199. Englewood Cliffs, NJ, USA: Prentice Hall, 1991.

[33] P. Liutanakul, A.-B. Awan, S. Pierfederici, B. Nahid-Mobarakeh, and F. Meibody-Tabar, "Linear Stabilization of a DC Bus Supplying a Constant Power Load: A General Design Approach," *IEEE Trans. Power Electron.*, vol. 25, no. 2, pp. 475–488, Feb. 2010.

[34] J. Sun, "Impedance-Based Stability Criterion for Grid-Connected Inverters," *IEEE Trans. Power Electron.*, vol. 26, no. 11, pp. 3075–3078, Nov. 2011.

[35] T. Dragicevic, "Dynamic Stabilization of DC Microgrids With Predictive Control of Point-of-Load Converters," *IEEE Trans. Power Electron.*, vol. 33, no. 12, pp. 10872–10884, Dec. 2018.

Linglin Chen received his MSc degree in Electrical Engineering from Zhejiang University, Hangzhou, China, in 2016. He is currently working toward the Ph.D. degree with the Power Electronics, Machine & Control (PEMC) group in the University of Nottingham, U.K.

He was a visiting scholar with the Department of Energy Technology, Aalborg University, Aalborg, Denmark.

His current research interests include high power AC/DC converters, high current DC/DC power converters, model predictive control and power distribution system in more electric aircrafts.

Lyuyi Lin received the B.S. degree in electrical engineering in 2016 from Tongji University, Shanghai, China. She is currently working toward the Ph.D. degree in electrical engineering in Zhejiang University.

Her current research interests include differential power processing in photovoltaic applications and digital control of power converters.

This article has been accepted for publication in a future issue of this journal, but has not been fully edited. Content may change prior to final publication. Citation information: DOI 10.1109/TPEL.2019.2962838, IEEE Transactions on Power Electronics

Shuai Shao (M'17) received the B.S. degree from Zhejiang University, China, in 2010, and the Ph.D. degree in electrical and electronic engineering from the University of Nottingham, U.K., in 2015.

In 2015, he joined the College of Electrical Engineering, Zhejiang University, as a Lecturer. His research interests include solid-state transformers, bidirectional dc-dc converters, and fault detection in power converters. He has published more than 30 peer-reviewed technical papers.

He serves as a Guest Associated Editor of Journal of Emerging and Selected Topics in Power Electronics.

Fei Gao received his Ph.D. degree in Electrical Engineering from the Power Electronics, Machines, and Control (PEMC) Research Group, University of Nottingham, Nottingham, UK, in 2016. From 2016 to 2019, he has been with Department of Engineering Science, University of Oxford, UK as a postdoctoral researcher.

From Mar. 2010 to Sep. 2012, he has worked in Jiangsu Electric Power Research Institute, Nanjing, State Grid Corporation of China. Since July 2019 he joined Shanghai Jiao Tong University as an associate professor.

His current research interests include modelling, control, power management and stability of power electronics-enabled micro-grids and more electric transportation systems. Dr. Gao won the European Union Clean Sky Best PhD Award in 2017 and IET Control & Automation Runner Up PhD Award in 2018.

Zhenyu Wang received the B.S. degree in Electrical Engineering, from Chongqing University, Chongqing, China in 2012, and the M.S. and Ph.D. degrees in Power Electronics from the University of Nottingham, Nottingham, UK, in 2014 and 2018, respectively.

He was a visiting scholar with the LEMUR Research Group at the University of Oviedo, Spain, from April 2016 to February 2017. He is currently a Research Fellow with the Power Electronics, Machines and Control (PEMC) Group at the University of Nottingham, Nottingham, UK.

His Research interests include SiC and GaN devices and applications, DC-DC converters for marine and aerospace applications, magnetic components for power electronic converters and power converter control.

Patrick Wheeler (SM'11) received his BEng [Hons] degree in 1990 from the University of Bristol, UK. He received his PhD degree in Electrical Engineering for his work on Matrix Converters from the University of Bristol, UK in 1994.

In 1993 he moved to the University of Nottingham and worked as a research assistant in the Department of Electrical and Electronic Engineering. In 1996 he became a Lecturer in the Power Electronics, Machines and Control Group at the University of Nottingham, UK. Since January 2008 he has been a Full Professor in the same research group. He is currently Head of the Department of Electrical and Electronic Engineering at the University of Nottingham and the Li Dak Sum Chair Professor in Electrical and Aerospace Engineering at the University of Nottingham, China. He is a member of the IEEE PELs AdCom and was an IEEE PELs Distinguished Lecturer from 2013 to 2017. He has published 500 academic publications in leading international conferences and journals.

Tomislav Dragičević (S'09-M'13-SM'17) received the M.Sc. and the industrial Ph.D. degrees in Electrical Engineering from the Faculty of Electrical Engineering, Zagreb, Croatia, in 2009 and 2013, respectively. From 2013 until 2016 he has been a Postdoctoral research associate at Aalborg University, Denmark. From March 2016 he is an Associate Professor at Aalborg University, Denmark where he leads an Advanced Control Lab.

He made a guest professor stay at Nottingham University, UK during spring/summer of 2018. His principal field of interest is design and control of micro-grids, and application of advanced modeling and control concepts to power electronic systems. He has authored and co-authored more than 155 technical papers (more than 70 of them are published in international journals, mostly IEEE Transactions) in his domain of interest, 8 book chapters and a book in the field.

He serves as Associate Editor in the IEEE TRANSACTIONS ON INDUSTRIAL ELECTRONICS, in IEEE Emerging and Selected Topics in Power Electronics and in IEEE Industrial Electronics Magazine. Dr. Dragičević is a recipient of the Končar prize for the best industrial PhD thesis in Croatia, and a Robert Mayer Energy Conservation award.